INORGANIC CHEMISTRY FRONTIERS

RESEARCH ARTICLE

View Article Online
View Journal | View Issue

Cite this: *Inorg. Chem. Front.*, 2023, **10**, 5710

Flexible strontium-based metal–organic framework scintillation screens for high-resolution X-ray imaging†

Peng-Kun Wang,[a,b,c] Wen-Fei Wang,[a,b,c] Bao-Yi Li,[a,b,c] Mei-Juan Xie,[a,b] Hong-Yi Bian,[a,b] Shuai-Hua Wang,[a,b] Fa-Kun Zheng *[a,b] and Guo-Cong Guo*[a,b]

Scintillators have been widely used in medical examinations, security inspections, aerospace and other applications with the ability to convert X-rays into UV/visible light. However, it remains a challenge to design and synthesize scintillators that feature low cost, high stability and easy preparation into flexible films. Here, we prepared a new 3D MOF $[Sr_2(DOBPDC)_2(DMF)]_n$ **1** by a short-cycle solvothermal method. Due to the synergistic contribution of the heavy metal and luminous organic functional motifs, compound **1** shows a higher X-ray responsive sensitivity than commercial scintillators BaF_2 and $PbWO_4$. The light yield of **1** is superior to those of some of our previously reported lead-based MOF scintillators at the same dose rates. The scintillation mechanism was elucidated using optical spectra and theoretical calculations. Benefiting from the strong connection between the metal atom and the rigid organic ligand, the structure and scintillation intensity of **1** remain almost unchanged while being immersed in water for 30 d, which confirms its outstanding water resistance. Meanwhile, the flexible scintillation screen **1-film** was prepared by knife coating, and X-ray imaging with a spatial resolution of 5 lp mm^{-1} was achieved. The **1-film** also shows high resistance to fatigue, irradiation and humidity, and also maintains favorable X-ray imaging quality after being stored under ambient conditions for 30 d. This work provides new insight for the design and synthesis of stable and efficient MOF-based scintillators used in flexible scintillation screens.

Received 2nd July 2023,
Accepted 17th August 2023

DOI: 10.1039/d3qi01231j

rsc.li/frontiers-inorganic

1. Introduction

Scintillators as the core of indirect X-ray detectors by converting X-ray photons into UV/visible light have been widely applied in medical imaging, public security, industrial nondestructive flaw detection and aviation detection.[1–3] The traditional inorganic scintillators such as CsI:Tl, $Bi_4Ge_3O_{12}$(BGO), $PbWO_4$(PWO) and $YAlO_3$:Ce are grown as solid block materials under harsh and costly preparation conditions,[4] which cannot meet the requirement of flexible imaging of non-planar objects (*e.g.* oral examination).[5,6] Organic scintillators composed of light atoms, such as C, N and O, result in poor X-ray absorption and relatively low scintillation intensity in spite of the advantages of easy preparation of flexible films, simple synthesis and fast decay time.[7] Perovskites are considered as highly promising scintillators due to their high light yield, but their instability towards water and oxygen hinders their practical applications in X-ray detection and imaging.[8,9] Therefore, it is a great challenge and an urgent requirement to explore scintillators used to prepare flexible films with high performance, excellent stability and easy manufacture.

Metal–organic frameworks (MOFs) are crystalline materials assembled from inorganic units and organic ligands by coordinate bonds, which have features of functional tunability, structural designability and mild synthesis processes.[10] By combining the respective advantages of the metal and organic ligand, scintillation MOFs (SMOFs) have the merits of high stability and easy film formation with polymer substrates, which is expected to help achieve the fabrication of economical, stable and flexible scintillation screens.[11] Moreover, the diverse choices of metal atoms and organic ligands provide enormous possibilities of various structures and properties. Therefore,

[a]*State Key Laboratory of Structural Chemistry, Fujian Institute of Research on the Structure of Matter, Chinese Academy of Sciences, Fuzhou 350002, P. R. China. E-mail: zfk@fjirsm.ac.cn, gcguo@fjirsm.ac.cn*
[b]*Fujian Science & Technology Innovation Laboratory for Optoelectronic Information of China, Fuzhou, Fujian 350108, P. R. China*
[c]*University of Chinese Academy of Sciences, Beijing 100039, P. R. China*

†Electronic supplementary information (ESI) available: Radioluminescence spectra, UV-Vis absorption spectra, FT-IR spectra and powder XRD pattern of **1**. CCDC 2261586 for **1**. For ESI and crystallographic data in CIF or other electronic format see DOI: https://doi.org/10.1039/d3qi01231j

the development of SMOF-based scintillation screens is feasible and promising. It has been revealed that the organic compound 3,3′-dihydroxy-4,4′-biphenyldicarboxylic acid (H_2DOBPDC) shows strong luminescence, and also MOFs constructed with H_2DOBPDC usually have robust structures to resist light, heat and moisture, which satisfies the demand for building stable H_2DOBPDC-based SMOFs.[12–14] On the other hand, most of the currently reported SMOFs contain toxic heavy metals, such as Pb, which is prone to pose a threat to human and biological systems.[15] It is necessary to select non-toxic or almost non-toxic heavy metals as substitutes for toxic heavy metals in SMOFs. Non-toxic elemental strontium not only has a relatively large atomic number, but due to its multiple coordination sites, the MOFs constructed with it tend to form dense structures, which are expected to facilitate the absorption of X-rays and photoelectron transfer.[16]

Based on the above considerations, a 3D Sr-based SMOF $[Sr_2(DOBPDC)_2(DMF)]_n$ **1** was synthesized *via* a low-cost and short-cycle solvothermal method. By synergizing the strong X-ray absorption by inorganic heavy metals with the excellent luminescence of organic ligands, compound **1** exhibits remarkable radioluminescence (RL) intensity. It is worth mentioning that the detection sensitivity of **1** exceeds those of commercial scintillators BaF_2 and PWO. The light yield of **1** is higher than those of some of our previously reported Pb-based SMOFs at the same dose rate of 42.29 mGy s^{-1}. Moreover, **1** shows high resistance to irradiation or fatigue, and maintains its structure and RL intensity after being immersed in water for 30 d, ensuring long-term stable operation. With the excellent scintillation sensitivity and prominent stability of **1**, the flexible scintillation screen **1-film** was prepared for X-ray imaging. The **1-film** can reach a relatively high spatial resolution of 5 lp mm^{-1}, and can still maintain satisfactory X-ray imaging performance after being stored in an air environment for 30 d. This work reports a new candidate scintillator for X-ray detection, provides a new insight for designing stable and efficient MOF-based scintillators employed in flexible scintillation screens and verifies the flexible scintillation screen applied in non-planar objects.

2. Experimental section

2.1 Synthesis

All reagents and solvents for the syntheses and analyses were commercially available and used as received. A mixture of the ligand H_2DOBPDC (0.05 mmol) and $Sr(NO_3)_2$ (0.05 mmol) was loaded into a heavy-wall glass tube. *N*,*N*-Dimethylformamide (3 mL), methanol (3 mL) and H_2O (1 mL) were added to the mixture. The tube was then sealed and heated at 120 °C in a programmable oven for 2 d, followed by slow cooling (0.1 °C min^{-1}) to room temperature. Colorless transparent crystals suitable for single-crystal X-ray diffraction were formed (75% yield based on $Sr(NO_3)_2$). Anal. calcd (%) for $C_{31}H_{23}NO_{13}Sr_2$: C 46.97, H 2.92, N 1.77. Found (%): C 46.60, H 2.99, N 1.76.

2.2 X-ray crystallography

Single-crystal X-ray diffraction data of **1** were obtained using a Rigaku FR-X Microfocus diffractometer equipped with a graphite monochromated Cu K_α radiation source (λ = 1.54184 Å) at 293 K. The intensity data sets were obtained using a ω-scan technique and reduced using CrystalClear software. The structure was solved by direct methods, and refined by full-matrix least-square on F^2 using the Olex2 1.5 software. The hydrogen atoms were calculated in idealized positions and refined with a riding model. All non-hydrogen atoms were refined anisotropically. Pertinent crystal data and structure refinement details for **1** are summarized in Table S1† and selected bond lengths and bond angles are given in Table S2.†

2.3 Physical characterization

Elemental analyses (C, H and N) were performed on an Elementar Vario EL III micro-analyzer. Thermogravimetric analysis (TGA) measurements and differential scanning calorimetry (DSC) experiments were carried out on a METTLER TOLEDO analyzer under a N_2 atmosphere and the sample was heated in an Al_2O_3 crucible at a heating rate of 10 K min^{-1}. The FT-IR spectra were collected on a VERTEX 70 spectrometer using KBr pellets in the range of 4000–400 cm^{-1}. Powder X-ray diffraction (PXRD) patterns were collected on a Rigaku Miniflex 600 diffractometer using Cu K_α radiation (λ = 1.5406 Å) in the 2θ range of 5–65°. The simulated patterns were produced using the Mercury version 4.2.0 software. UV-Vis absorption spectra were obtained in the reflectance mode at room temperature on a PerkinElmer Lambda 950 spectrophotometer with $BaSO_4$ as a reference. The SEM images were recorded on a Zeiss Sigma 300 field emission scanning electron microscope. The used accelerating voltage is 3 kV.

2.4 Scintillating luminescence and X-ray imaging

RL spectra were collected on a self-built X-ray stimulated Edinburgh FLS920 Fluorescence Spectrometer with a highly purified tungsten target (5 W) as the excitation source and PMT (HAMAMATSU R928) as the detector. The samples were placed compactly in a quartz-capped copper plate with a certain volume of $\pi \times (5\ mm)^2 \times 2$ mm. Both the spot of the X-ray and the fibre optic spectrometer can completely cover the samples. The fibre optic spectrometer was then used to collect emission spectra with excitation by X-rays. A lead box serves as an X-ray protective device. The light yield (LY) of BGO is 8000 photons per MeV, and the LYs were estimated according to the equation $LY = S_{sample}/S_{BGO} \times 8000$, where S is the integral area of the X-ray excited luminescence (RL) spectrum.[17–19] The X-ray images were acquired by using a digital camera (Canon 5D4) under 50 kV X-ray irradiation.

2.5 Luminescence measurements

The photoluminescence (PL) spectra were collected on an Edinburgh FLS920 fluorescence spectrometer equipped with a 450 W xenon lamp as the excitation source. Luminescence lifetimes and photoluminescence quantum yield (PLQY) tests

were carried out on an Edinburgh FLS1000 UV/Vis/NIR fluorescence spectrometer.

2.6 Calculation of electronic structures and density of states (DOS)

The calculation model of **1** was built directly from single-crystal X-ray diffraction data. Calculations of electronic structures and DOS were performed with the DMol^3 code based on DFT with the GGA-PBE functional in the Materials Studio v8.0 software package.

2.7 Attenuation efficiency calculation

The attenuation efficiency T is defined by the following equation:

$$T = 1 - e^{-\mu_L x}$$

In this equation, x is the thickness of the material. The μ_L value is the linear attenuation coefficient that is defined as $\mu_L = \rho\mu_m$, where ρ is the density of the material and μ_m is the mass attenuation coefficient. The value of μ_m is obtained from the XCOM photon cross section database (**https://physics.nist.gov/PhysRefData/Xcom/html/xcom1.html**).

2.8 Preparation of the 1-film

The crystals of **1** were ground and sieved into microcrystals with the size less than 50 μm. The microcrystals of **1** (400 mg) and polyvinylidene fluoride (PVDF) (200 mg) were added to DMF (1.5 mL) in a beaker. A homogeneous mixture was obtained by stirring and sonication. The above mixed solution was evenly knife coated onto the cleaned polyethylene terephthalate (PET) substrate and cured at room temperature, and a 6 × 5 cm^2 (thickness of about 100 μm) flexible film was obtained.

2.9 Hygroscopy experiments

The water resistance of **1** was measured by completely immersing crystals in a beaker which was filled with water. After being soaked for different times, a small amount of the samples were removed each time for PXRD test and scintillation characterization.

At a given temperature, the atmosphere of a saturated salt solution has a definite relative humidity. The relative humidity of 85% was obtained from the saturated solution of KNO_3 at 298 K. The control **1-film** was secured by wire under an 85% relative humidity atmosphere for 3 d. The RL spectra of the **1-film** induced by X-rays were recorded for comparison.

3. Results and discussion

3.1 Crystal structure and fundamental characterization

Single crystal X-ray diffraction analysis shows that **1** crystallizes in the monoclinic space group *C*2/*c*. The asymmetric unit includes one Sr^{2+} ion, one DOBPDC^{2-} ligand, and one half-occupied coordinated DMF molecule (Fig. 1a). Each DMF molecule possesses a symmetric plane through an O1 atom.

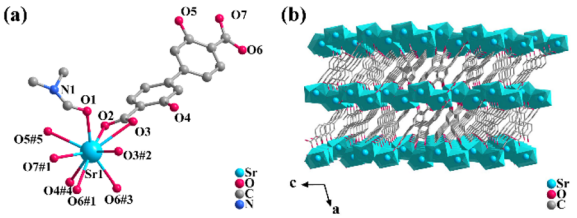

Fig. 1 (a) The coordination environment of Sr^{2+} centers in **1**. (b) The 3D frame aggregation along the *b*-axis of **1**. Symmetry codes: #1 –1/2 + *x*, 1/2 + *y*, –1 + *z*; #2 1 – *x*, *y*, 1/2 – *z*; #3 3/2 – *x*, 1/2 – *y*, 1 – *z*; #4 *x*, 1 – *y*, –1/2 + *z*; #5 3/2 – *x*, 3/2 – *y*, 1 – *z*.

The DOBPDC^{2-} ligand adopts a μ_6-bridging mode to link Sr atoms (Fig. S1a†), and each carboxylate group takes a μ_2–η^2:η^1 style (Fig. S1b†) to connect two Sr atoms. Each hydroxyl group is coordinated to one Sr atom. Each Sr^{2+} ion is coordinated by nine O atoms, including four from two carboxylate groups in a chelate mode, two from two carboxylate groups with η^2 oxygens, two from protonated hydroxyl groups, and one from a DMF molecule (Fig. S2†). The Sr–O bond lengths are within a reasonable range of 2.604(18)–2.955(17) Å. The different Sr^{2+} ions are linked by the η^2 oxygens (O6#1, O6#3, O3, and O3#2) and the oxygens (O1) in DMF, forming a 1D metallic oxygen chain extending indefinitely along the *c*-axis (Fig. S3a†). The adjacent 1D chains are linked *via* the coordination of Sr^{2+} to the carboxyl and the hydroxyl oxygens on the same side, respectively, resulting in the formation of a 2D layer parallel to the *bc* plane (Fig. S3b†), which further stacks up *via* hydroxyl oxygens and μ_2–η^2:η^1 mode of two terminal carboxyl groups from different ligands into a dense 3D network (Fig. 1b). Due to the strong electronegativity of the O atom, the carboxylate oxygen of the ligand forms hydrogen bonds with the hydroxyl hydrogen in the range of 1.859–1.910 Å (Fig. S1a†) within the molecule, which further guarantees the stability of the crystal structure.

The purity and composition of the as-synthesized crystal **1** were confirmed by powder X-ray diffraction (PXRD) and FT-IR spectra (Fig. S4 and S5†). The TGA & DSC curves of **1** (Fig. S6†) indicate a relatively superior thermal stability.

3.2 X-ray scintillation properties

The RL spectrum of **1** was measured to explore the X-ray detection capability. Compound **1** emits a characteristic blue emission peak at 430 nm by X-ray excitation (Fig. S7†). The RL spectra of **1** at different radiation dose rates from 0.69 to 42.29 mGy s^{-1} were systematically recorded by fixing the tube voltage of the X-ray source at 50 kV and varying the tube current to change the dose rate (Fig. S7†). The RL intensity of **1** increases continuously with the rising X-ray dose rate, which reveals an efficient X-ray response. In order to eliminate the possible effects of the raw reactants on the radiation detection performance, compound **1** and the raw reactants were tested for RL intensities at the same dose rate of 42.29 mGy s^{-1}. The raw reactants, including the free ligand, the metal salt Sr $(NO_3)_2$, and the corresponding equimolar mechanical mixtures

of the free ligand and the metal salt, all showed rather weak RL intensities (Fig. 2a). Compared to the equimolar mechanical mixture of the free ligand and the metal salt, the RL intensity of **1** increased by nearly 20 times. This result demonstrates that **1** could effectively combine the advantages of both the strong X-ray blocking ability of the heavy metal and the strong luminescence properties of the organic ligand to exhibit strong X-ray responsive radioluminescence.

In addition, in order to characterize the scintillation performance of **1**, some conventional scintillators (BGO, BaF_2, PWO and organic crystal anthracene) and two of our previously reported Pb-based SMOFs (Pb-SMOF-1[20] and Pb-SMOF-2[21]) serve as references. The RL intensities of **1** and the reference samples both display the favourable linearity with the increasing dose rate (Fig. 2b). The linear relationship of **1** shows a larger slope than the other samples except BGO, implying a higher X-ray responsive sensitivity, which suggests that **1** can be used as a highly sensitive scintillator. The higher sensitivity facilitates a more sensitive response in X-ray detection and guarantees a high-resolution X-ray image. The LYs were calculated to intuitively quantify the scintillation performance of **1**. The LY of **1** is 3223 photons per MeV, which is higher than those of BaF_2, PWO, organic anthracene, Pb-SMOFs-1 and Pb-SMOF-2 at the same dose rate of 42.29 mGy s^{-1} (Fig. S8† and Fig. 2c). The limit of detection (LOD) of scintillators defined as the dose rate when the signal to noise ratio (SNR) ≥ 3.[22] The LOD of **1** is 4.96 μGy s^{-1} (Fig. 2d), which is slightly lower than the requirement for medical diagnosis (5.50 μGy s^{-1}).[23]

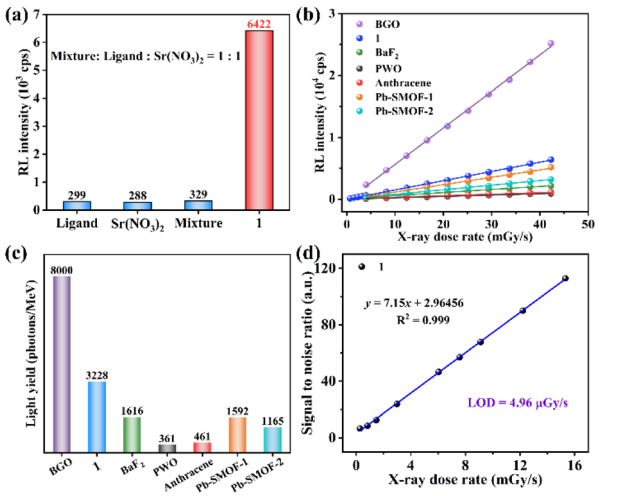

Fig. 2 (a) RL intensity of raw reactants, including the ligand, $Sr(NO_3)_2$ and a physical mixture of $Sr(NO_3)_2$ and the ligand (the molar ratio is 1 : 1), and **1** under a dose rate of 42.29 mGy s^{-1}. (b) The linear relationship between RL intensity and X-ray dose rates of **1**, BGO, PWO, BaF_2, organic crystal anthracene and reported Pb-based SMOFs (Pb-SMOF-1 and Pb-SMOF-2). (c) The comparison of light yields between **1**, the conventional scintillators (BGO, BaF_2, PWO and organic crystal anthracene) and some reported Pb-based SMOFs (Pb-SMOF-1 and Pb-SMOF-2) tested at the same dose rate of 42.29 mGy s^{-1}. (d) The detection limit is **1**.

The water resistance of scintillators is an essential prerequisite for its long-term and stable operation, which is a dilemma for some commercial scintillators (CsI:Tl) and perovskite-based scintillators.[24] Compound **1** retained its structural stability, and showed almost unanimous X-ray responsive scintillation sensitivities after being immersed in water for 30 d, demonstrating excellent water tolerance (Fig. 3a, b and Fig. S9†). Such outstanding water resistance can be attributed to the strong bonding between the metal atom and the rigid ligand, which effectively resists water erosion and prevents further decomposition of the crystals.[25]

Continuous X-ray irradiation tends to cause a degradation of the material performance.[26] After a continuous X-ray irradiation at a high dose rate of 42.29 mGy s^{-1} for 2 h with a cumulative dose of ~330 Gy, there is almost no change in RL intensity (Fig. 3c). In addition, the intensity, peak position and shape of the RL spectra remained almost constant at a dose rate of 42.29 mGy s^{-1} measured every 20 min (Fig. 3d). Meanwhile, the RL intensity remained almost identical after 100 on/off operations at an irradiation dose of 42.29 mGy s^{-1} and a total irradiation time of 2000 s (Fig. S10†), reflecting the good fatigue resistance and long-term operational stability.

3.3 Scintillation mechanism

In order to elucidate the scintillation mechanism, the optical properties of **1** and the free ligand were investigated. The solid-state UV-Vis absorption spectra at room temperature (Fig. S11†) show that the free ligand and **1** exhibit the same absorption range and parallel shapes in the UV-Vis region in the range of 250–400 nm, which can be attributed to the ligand-based n → π* or π → π* transition. Compound **1** shows a bright blue light emission peak at 430 nm under 345 nm excitation (Fig. 4a and Fig. S12†), giving CIE coordinates (0.151, 0.071) (Fig. S13†). The free ligand H_2DOBPDC shows an emission peak at 445 nm under 368 nm excitation which is

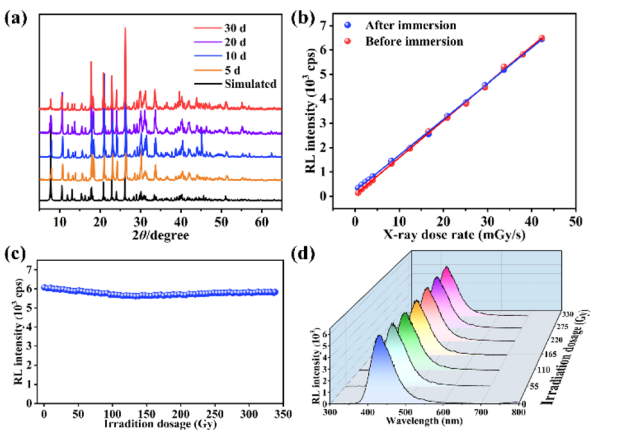

Fig. 3 (a) The PXRD patterns of **1** immersed in water for different time periods. (b) The sensitivities of **1** before and after being immersed in water for 30 d. The tendency chart of the X-ray responsive intensity (c) and the RL spectra (d) of **1** *versus* irradiation doses at a dose rate of 42.29 mGy s^{-1}.

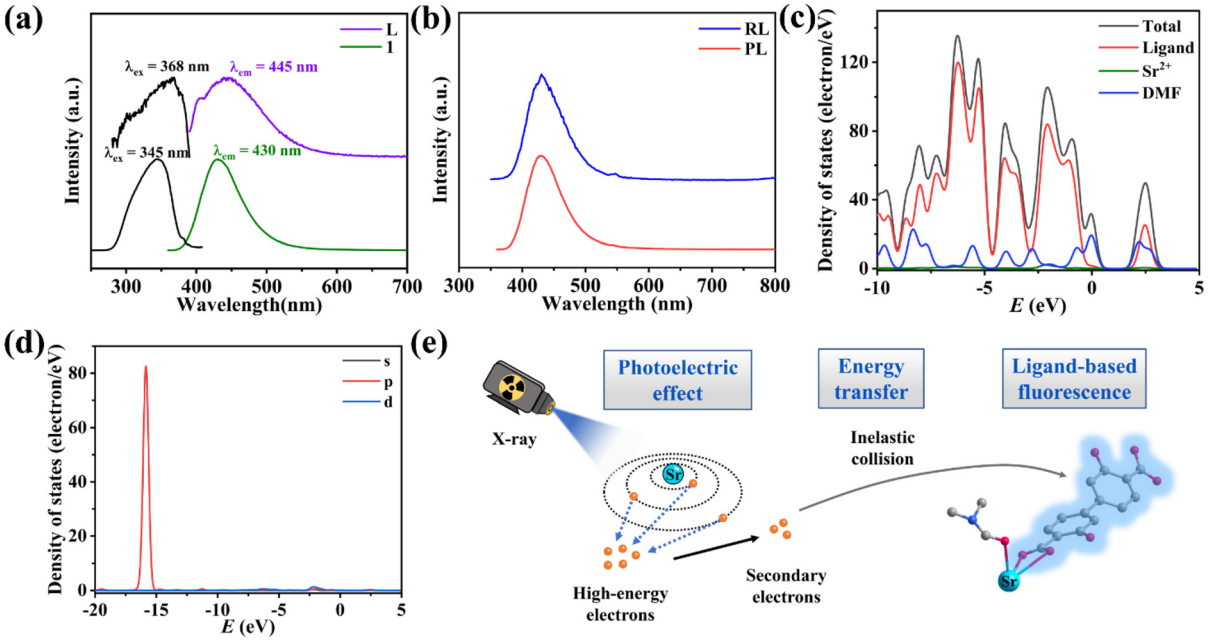

Fig. 4 (a) The solid-state PL excitation and emission spectra of H_2DOBPDC and **1**. (b) The PL and RL spectra of **1**. (c) Profile of the total/partial electronic density of states of **1**. (d) The partial electronic density of states of Sr^{2+}. (e) Diagram of the RL mechanism of **1**.

parallel to the shape of the PL spectrum of **1** (Fig. 4a), meaning that the photophysical mechanism of **1** is mainly from ligand-centred fluorescence emission. Meanwhile, the PL emission peaks of **1** and H_2DOBPDC are almost unchanged with varying excitation wavelength (Fig. S14†). Compound **1** displays a larger Stokes shift compared to the free ligand, which can effectively reduce the self-absorption and is beneficial in achieving strong luminescence and scintillation. The fluorescence lifetime of **1** is 1.86 ns (Fig. S15†), typical of fluorescence emission. Such a rapid fluorescence decay lifetime would ensure a fast decay of the scintillation intensity, which facilitates the reduction of the scintillation afterglow. The photoluminescence quantum yield (PLQY) of **1** reaches 18.55%, affording strong scintillation ability.

To explore the scintillation mechanism, the PL and RL spectra of **1** were compared. The peak positions of the RL and PL spectra are identical, while the peak shapes are perfectly parallel (Fig. 4b), which proves that the fluorescence and scintillation originate from a similar emission process.

To better investigate the contribution of electrons from different components, the total and partial densities of states (TDOS and PDOS) of **1** were studied based on crystallographic data in the DMol^3 mode at the GGA/PBE level. As shown in Fig. 4c, Sr^{2+} contributes a little to the valence band (VB) top and conduction band (CB) bottom. The energies of the VBs lie between −10.00 and 0.00 eV and the CBs originate almost from the p orbital of the ligand $DOBPDC^{2-}$. In addition, the coordinated DMF molecules have little contribution to VBs and CBs, which could be involved in the energy transfer of non-radiative transition, consuming a part of the energy. The p-orbital of Sr^{2+} has a distinct contribution of the deep valence band in the energy range from −16.64 to −14.94 eV (Fig. 4d). Thus, the high-energy penetrating X-ray can excite the deep energy level electrons of Sr^{2+} ions. Combined with the dramatically different RL intensities of **1** and the free ligand, the scintillation of **1** probably stems mainly from ligand-based electron transitions induced by the metal Sr^{2+} absorption of X-ray photons.[8,20]

The scintillation efficiency in SMOFs is closely related to the following three factors: excitation and conversion (β), energy transfer process (S) and luminescence yield (Q).[27,28] The scintillation of **1** should undergo the following processes: firstly, the relatively heavy metal Sr^{2+} acts as a suitable X-ray absorbing antenna and interacts with the incident X-ray through the photoelectric effect, generating a large number of high-energy electrons. Then, the high-energy electrons are rapidly thermally activated to secondary electrons, which further transfer energy to the luminescent organic ligand $DOBPDC^{2-}$ through inelastic scattering, bringing the electrons to excited states. Finally, the electrons in the excited states decay to the ground states through radiative transition to generate scintillation fluorescence (Fig. 4e).[29]

The process of β depends on the X-ray absorption ability of the materials. The mass attenuation coefficients and the X-ray attenuation efficiencies of **1** and the reported Pb-based SMOFs were calculated to compare the β efficiency (Fig. S16†).[30] It is shown that the X-ray absorption and blocking abilities of **1** are relatively weaker compared to those of Pb-based SMOFs. However, compound **1** exhibits higher LY than Pb-SMOF-1 and Pb-SMOF-2, which could be attributed to the S of **1** being more effective. The dense structure of **1** could increase the probability of inelastic collisions of secondary electrons and reduce

energy dissipation by non-radiative transition.[31,32] In addition, the high PLQY of **1** facilitates the *Q* of the scintillation process, which may be another reason for the stronger scintillation intensity of **1**.[33]

3.4 Flexible X-ray devices and imaging

The high detection sensitivity and outstanding stability of **1** can support film preparation for X-ray imaging. Compound **1** is well compatible with the PVDF, widely used for the preparation of flexible scintillation screens.[34–36] Powdered **1** was mixed with a PVDF substrate to obtain the **1-film** with favourable flexibility, which emitted uniform blue light under UV lamp excitation (Fig. 5a). The X-ray dose rate dependent RL spectra show that the **1-film** has an excellent linear relationship between the X-ray responsive RL intensity and dose rate (Fig. S17†). The RL spectra of the **1-film** exhibit an almost unanimous peak pattern as **1** without the effects of redundant emissions, although there is a decrease in its RL intensity (Fig. S18†). Scanning electron microscopy (SEM) results show that the microcrystals of **1** are compactly distributed in the PVDF, forming a uniform **1-film** surface, which facilitates high-resolution imaging (Fig. S19†).

In order to demonstrate the X-ray imaging quality of the **1-film**, the self-built imaging system is shown in Fig. 5b. To measure the spatial resolution of the flexible screen, the line pair card was applied to X-ray imaging tests (Fig. 5c). With the contrast statistics for the contour edges of the line pair card strip pattern, modulation transfer function (MTF) values at different resolutions were obtained. The flexible screen displays a spatial image resolution of 5 line pairs per millimeter (lp mm^{-1}) at an MTF of 0.21 (Fig. 5d), which is equivalent to those of the commercial CsI:Tl and α-Se flat panel detector (≥4 lp mm^{-1}@MTF 0.2).[37] Furthermore, the spring inside the capsule and the internal structure of the electronic component are clearly visible (Fig. 5e), demonstrating the ability of the **1-film** to achieve a high imaging quality. The flexible screens can better fit the nonplanar objects tightly, which is beneficial for reducing imaging distortion.[19,38] Compared with the relatively blurred X-ray radiograph of curved wires with the planar **1-film** (Fig. S20†), the internal structures of the curved wires are clearly visible with the flexible **1-film** with different curvature radii (Fig. 6a and b). It demonstrates the high spatial resolution of the bent **1-film**, proving the potential of the X-ray imaging ability for non-planar objects.

In addition, the RL intensity of the **1-film** demonstrated no significant reduction (Fig. S21†) after irradiation for up to 2 h and still maintained high quality imaging (Fig. 6c). We further placed the **1-film** in a humidity bottle at 85% relative humidity (Fig. 6d) for 3 d, showing no significant change in the RL intensity and the X-ray imaging performance (Fig. S22† and Fig. 6e). The scintillation intensities of the **1-film** remained almost unchanged after 120 on/off cycles of continuous X-ray switching (Fig. S23†), verifying the fast response to X-ray photons, indicating the favourable irradiation and fatigue resistance. After 30 d under ambient conditions (20–35 °C, 40–65% humidity), the **1-film** still retained its RL intensity and outstanding imaging capability (Fig. S22 and S24†), showing good stability against water and oxygen degradation. Therefore, the **1-film** flexible scintillation screen is capable of achieving high-resolution X-ray imaging.

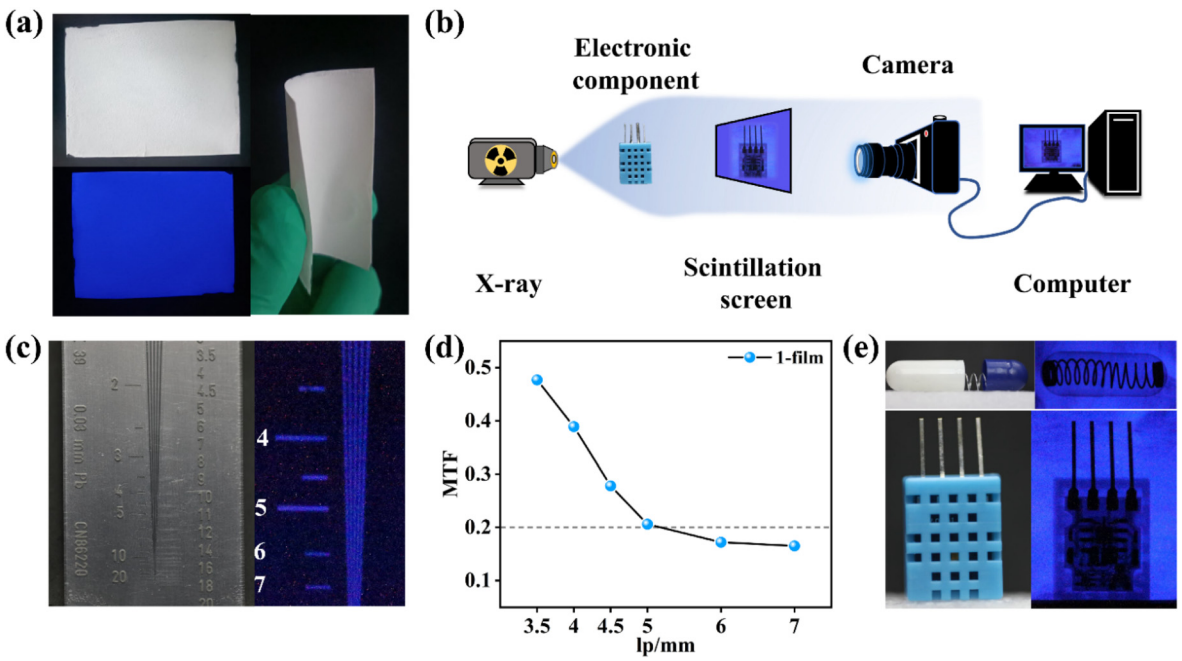

Fig. 5 (a) The photographs of the flexible **1-film**. (b) The schematic diagram of the self-built X-ray imaging system. (c) Photograph of real line pair card and its X-ray radiograph. (d) The MTF value of the **1-film** by the line-pair pattern method. (e) The real pictures and X-ray radiographs of the capsule and electronic component.

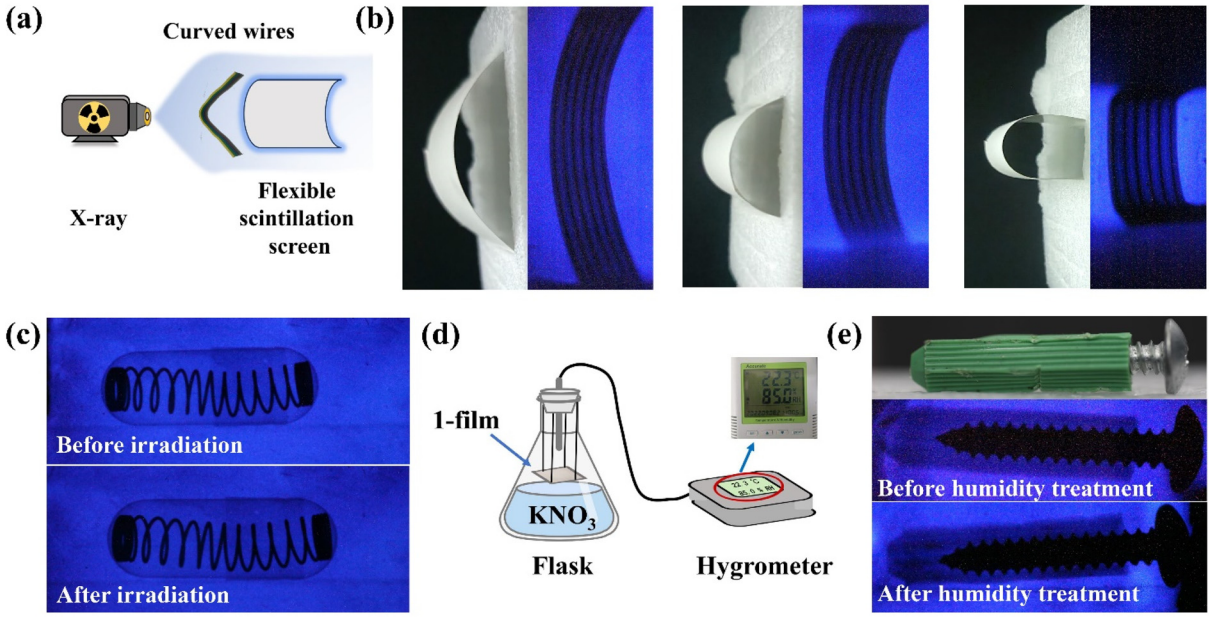

Fig. 6 (a) The schematic diagram of X-ray imaging with the flexible scintillation screen. (b) The real pictures of the **1-film** with different curvature radii and the X-ray radiographs of curved wires with different curvature radii of the **1-film**. (c) The X-ray radiographs before and after continuous X-ray irradiation. (d) The diagram of the humidity handling unit. (e) The physical photograph and X-ray radiographs before and after the humidity treatment.

4. Conclusions

In conclusion, based on the synergistic effect of the non-toxic heavy atom Sr with efficient X-ray absorption and rigid organic ligand $DOBPDC^{2-}$ with strong luminescence ability, a dense 3D SMOF $[Sr_2(DOBPDC)_2(DMF)]_n$ **1** has been synthesized by the solvothermal method. Compound **1** displays bright blue emissions under UV or X-ray irradiation with a rapid decay time of 1.86 ns, beneficial for effectively weakening the luminous trailing. Strong X-ray responsive RL intensity and detection sensitivity were observed in **1**, which is superior to those of commercial scintillators BaF_2, PWO and organic crystal anthracene. A low detection limit of 4.96 μGy s^{-1} meets the demands of X-ray medical diagnosis. The scintillation mechanism was elucidated with the aid of optical spectra and theoretical calculations. The flexible scintillation screen **1-film** was manufactured to achieve high-quality imaging with a spatial resolution of 5 lp mm^{-1}@MTF 0.21, which is comparable to that of the commercial CsI:Tl or α-Se flat panel detector. The potential of the **1-fim** for flexible X-ray imaging of non-planar objects was verified. Stability tests show that compound **1** and the **1-film** have excellent resistance to continuous radiation, heating, fatigue, water and humidity, which may be attributed to strong coordination bonds, suggesting good prospects for long-term practical applications. This work develops a new candidate scintillator for X-ray detection and imaging, and supplies a new insight for designing stable MOF-based scintillators for X-ray detection and preparing flexible scintillation screens for X-ray imaging. Further improvement of the scintillating performance of MOF crystals is the target we struggle for in the future work.

Author contributions

Peng-Kun Wang designed, synthesized compounds, and wrote the draft. Wen-Fei Wang assisted in crystal structure analysis, analyzed experimental results, and revised the manuscript. Bao-Yi Li, Mei-Juan Xie, and Hong-Yi Bian assisted in testing. Shuai-Hua Wang assisted in the DFT calculations and revised the manuscript. Fa-Kun Zheng conceived the experiments, analyzed and discussed the results, and revised the manuscript. Guo-Cong Guo revised the manuscript. All the authors have approved the final version of the manuscript.

Conflicts of interest

The authors declare that they have no known competing financial interests or personal relationships that could have appeared to influence the work reported in this paper.

Acknowledgements

This work was financially supported by the National Natural Science Foundation of China (21971240 and 22271283) and the Scientific Instrument Developing Project of the Chinese Academy of Sciences (YJKYYQ20210039). We sincerely thank

Prof. Shao-Fan Wu from Fujian Institute of Research on the Structure of Matter, Chinese Academy of Sciences, for the help with measurements.

References

1 Q. Chen, J. Wu, X. Ou, B. Huang, J. Almutlaq, A. A. Zhumekenov, X. Guan, S. Han, L. Liang, Z. Yi, J. Li, X. Xie, Y. Wang, Y. Li, D. Fan, D. B. L. Teh, A. H. All, O. F. Mohammed, O. M. Bakr, T. Wu, M. Bettinelli, H. Yang, W. Huang and X. Liu, All-inorganic perovskite nanocrystal scintillators, *Nature*, 2018, **561**, 88–93.

2 L. Lian, X. Wang, P. Zhang, J. Zhu, X. Zhang, J. Gao, S. Wang, G. Liang, D. Zhang, L. Gao, H. Song, R. Chen, X. Lan, W. Liang, G. Niu, J. Tang and J. Zhang, Highly luminescent zero-dimensional organic copper halides for X-ray scintillation, *J. Phys. Chem. Lett.*, 2021, **12**, 6919–6926.

3 P. Büchele, M. Richter, S. F. Tedde, G. J. Matt, G. N. Ankah, R. Fischer, M. Biele, W. Metzger, S. Lilliu, O. Bikondoa, J. E. Macdonald, C. J. Brabec, T. Kraus, U. Lemmer and O. Schmidt, X-ray imaging with scintillator-sensitized hybrid organic photodetectors, *Nat. Photonics*, 2015, **9**, 843–848.

4 X. Liu, R. Li, X. Xu, Y. Jiang, W. Zhu, Y. Yao, F. Li, X. Tao, S. Liu, W. Huang and Q. Zhao, Lanthanide(III)–Cu_4I_4 organic framework scintillators sensitized by cluster–based antenna for high–resolution X–ray imaging, *Adv. Mater.*, 2023, **35**, 2206741.

5 F. Zhang, Y. Zhou, Z. Chen, M. Wang, Z. Ma, X. Chen, M. Jia, D. Wu, J. Xiao, X. Li, Y. Zhang, Z. Shi and C. Shan, Thermally activated delayed fluorescence zirconium–based perovskites for large–area and ultraflexible X–ray scintillator screens, *Adv. Mater.*, 2022, **34**, 2204801.

6 L. Han, H. Zhang, Y. Ning, H. Chen, C. Guo, J. Cui, G. Peng, Z. Ci and Z. Jin, Environmentally stable one-dimensional copper halide based ultra-flexible composite film for low-cost X-ray imaging screens, *Chem. Eng. J.*, 2022, **430**, 132826.

7 J.-X. Wang, L. Gutiérrez-Arzaluz, X. Wang, M. Almalki, J. Yin, J. Czaban-Jóźwiak, O. Shekhah, Y. Zhang, O. M. Bakr, M. Eddaoudi and O. F. Mohammed, Nearly 100% energy transfer at the interface of metal-organic frameworks for X-ray imaging scintillators, *Matter*, 2022, **5**, 253–265.

8 X. Zhang, H. Qiu, W. Luo, K. Huang, Y. Chen, J. Zhang, B. Wang, D. Peng, Y. Wang and K. Zheng, High–performance X–ray imaging using lanthanide metal-organic frameworks, *Adv. Sci.*, 2023, 2207004.

9 Y. Li, Q.-L. Li, Y. Li, Y.-L. Yang, S.-L. Zhang, J. Zhao, J. Wan and Z. Zhang, Water-assistant ultrahigh fluorescence enhancement in perovskite polymer-encapsulated film for flexible X-ray scintillators, *Chem. Eng. J.*, 2023, **452**, 139132.

10 J. Xie, Y. Wang, W. Liu, X. Yin, L. Chen, Y. Zou, J. Diwu, Z. Chai, T. E. Albrecht-Schmitt, G. Liu and S. Wang, Highly sensitive detection of ionizing radiations by a photoluminescent uranyl organic framework, *Angew. Chem., Int. Ed.*, 2017, **56**, 7500–7504.

11 F. P. Doty, C. A. Bauer, A. J. Skulan, P. G. Grant and M. D. Allendorf, Scintillating metal-organic frameworks: a new class of radiation detection materials, *Adv. Mater.*, 2009, **21**, 95–101.

12 X. Liu, X. Wang, T. Gao, Y. Xu, X. Shen and D. Zhu, Three 3D lanthanide-organic frameworks with sra topology: syntheses, structures, luminescence and magnetic properties, *CrystEngComm*, 2014, **16**, 2779–2787.

13 H. Furukawa, F. Gándara, Y.-B. Zhang, J. Jiang, W. L. Queen, M. R. Hudson and O. M. Yaghi, Water adsorption in porous metal-organic frameworks and related materials, *J. Am. Chem. Soc.*, 2014, **136**, 4369–4381.

14 S. Peng, B. Bie, Y. Sun, M. Liu, H. Cong, W. Zhou, Y. Xia, H. Tang, H. Deng and X. Zhou, Metal-organic frameworks for precise inclusion of single-stranded DNA and transfection in immune cells, *Nat. Commun.*, 2018, **9**, 1293.

15 T. Xu, Y. Li, M. Nikl, R. Kucerkova, Z. Zhou, J. Chen, Y.-Y. Sun, G. Niu, J. Tang, Q. Wang, G. Ren and Y. Wu, Lead-free zero-dimensional organic-copper(I) halides as stable and sensitive X-ray scintillators, *ACS Appl. Mater. Interfaces*, 2022, **14**, 14157–14164.

16 M. A. Alnaqbi, A. Alzamly, S. H. Ahmed, M. Bakiro, J. Kegere and H. L. Nguyen, Chemistry and applications of s-block metal–organic frameworks, *J. Mater. Chem. A*, 2021, **9**, 3828–3854.

17 M. Li, Y. Wang, L. Yang, Z. Chai, Y. Wang and S. Wang, Circularly polarized radioluminescence from chiral perovskite scintillators for improved X-ray imaging, *Angew. Chem., Int. Ed.*, 2022, **61**, e202208440.

18 J.-X. Wang, Y. Wang, I. Nadinov, J. Yin, L. Gutiérrez-Arzaluz, O. Alkhazragi, T. He, T. K. Ng, M. Eddaoudi, H. N. Alshareef, O. M. Bakr, B. S. Ooi and O. F. Mohammed, Aggregation-induced fluorescence enhancement for efficient X-ray imaging scintillators and high-speed optical wireless communication, *ACS Mater. Lett.*, 2022, **4**, 1668–1675.

19 L. Yang, Z. Li, L. He, J. Sun, J. Wang, Y. Wang, M. Li, Z. Zhu, X. Dai, S. Hu, F. Zhai, Q. Yang, Y. Tao, Z. Chai, S. Wang and Y. Wang, Emergence of a lanthanide chalcogenide as an ideal scintillator for a flexible X-ray detector, *Angew. Chem., Int. Ed.*, 2023, e202306465.

20 W.-F. Wang, J. Lu, X.-M. Xu, B.-Y. Li, J. Gao, M.-J. Xie, S.-H. Wang, F.-K. Zheng and G.-C. Guo, Sensitive X-ray detection and imaging by a scintillating lead(II)-based metal-organic framework, *Chem. Eng. J.*, 2022, **430**, 133010.

21 M.-J. Xie, W.-F. Wang, B.-Y. Li, J. Gao, Y.-F. Yan, J. Lu, F.-K. Zheng and G.-C. Guo, A X-ray responsive scintillating coordination polymer constructed by lead(II) and anthracene derivative, *Inorg. Chem. Commun.*, 2022, **142**, 109711.

22 X. Xu, F. Wang, W. Xu, H. Lu, L. Lv, H. Sha, X. Jiang, S. Wu and S. Wang, Wide–bandgap rare–earth iodate single crystals for superior X–ray detection and imaging, *Adv. Sci.*, 2023, 2206833.

23 B. Yang, L. Yin, G. Niu, J. Yuan, K. Xue, Z. Tan, X. Miao, M. Niu, X. Du, H. Song, E. Lifshitz and J. Tang, Lead–free

halide Rb_2CuBr_3 as sensitive X–ray scintillator, *Adv. Mater.*, 2019, **31**, 1904711.

24 R. Duan, Z. Chen, D. Xiang, J. Si and X. Liu, Large-area flexible scintillator screen based on copper-based halides for sensitive and stable X-ray imaging, *J. Lumin.*, 2023, **253**, 119482.

25 S. Yuan, L. Feng, K. Wang, J. Pang, M. Bosch, C. Lollar, Y. Sun, J. Qin, X. Yang, P. Zhang, Q. Wang, L. Zou, Y. Zhang, L. Zhang, Y. Fang, J. Li and H.-C. Zhou, Stable metal-organic frameworks: stable metal-organic frameworks: design, synthesis, and applications, *Adv. Mater.*, 2018, **30**, 1870277.

26 Y. Wang, X. Liu, X. Li, F. Zhai, S. Yan, N. Liu, Z. Chai, Y. Xu, X. Ouyang and S. Wang, Direct radiation detection by a semiconductive metal-organic framework, *J. Am. Chem. Soc.*, 2019, **141**, 8030–8034.

27 J. Lu, S.-H. Wang, Y. Li, W.-F. Wang, C. Sun, P.-X. Li, F.-K. Zheng and G.-C. Guo, Heat-resistant Pb(II)-based X-ray scintillating metal-organic frameworks for sensitive dosage detection via an aggregation-induced luminescent chromophore, *Dalton Trans.*, 2020, **49**, 7309–7314.

28 P. Lecoq, A. Gektin and M. Korzhik, Inorganic scintillators for detector systems, in *Physical Principles and Crystal Engineering*, Springer Press, 2017.

29 C. Wang, O. Volotskova, K. Lu, M. Ahmad, C. Sun, L. Xing and W. Lin, Synergistic assembly of heavy metal clusters and luminescent organic bridging ligands in metal-organic frameworks for highly efficient X-ray scintillation, *J. Am. Chem. Soc.*, 2014, **136**, 6171–6174.

30 Y. Wang, X. Yin, W. Liu, J. Xie, J. Chen, M. A. Silver, D. Sheng, L. Chen, J. Diwu, N. Liu, Z. Chai, T. E. Albrecht-Schmitt and S. Wang, Emergence of uranium as a distinct metal center for building intrinsic X-ray scintillators, *Angew. Chem., Int. Ed.*, 2018, **57**, 7883–7887.

31 J. Perego, I. Villa, A. Pedrini, E. C. Padovani, R. Crapanzano, A. Vedda, C. Dujardin, C. X. Bezuidenhout, S. Bracco, P. E. Sozzani, A. Comotti, L. Gironi, M. Beretta, M. Salomoni, N. Kratochwil, S. Gundacker, E. Auffray, F. Meinardi and A. Monguzzi, Composite fast scintillators based on high-*Z* fluorescent metal–organic framework nanocrystals, *Nat. Photonics*, 2021, **15**, 393–400.

32 J.-C. Jin, Y.-P. Lin, D.-Y. Chen, B.-Y. Lin, T.-H. Zhuang, W. Ma, L.-K. Gong, K.-Z. Du, J. Jiang and X.-Y. Huang, X-ray scintillation and photoluminescence of isomorphic ionic bismuth halides with $[Amim]^+$ or $[Ammim]^+$ cations, *Inorg. Chem. Front.*, 2021, **8**, 4474–4481.

33 M. Leng, Y. Yang, Z. Chen, W. Gao, J. Zhang, G. Niu, D. Li, H. Song, J. Zhang, S. Jin and J. Tang, Surface passivation of bismuth-based perovskite variant quantum dots to achieve efficient blue emission, *Nano Lett.*, 2018, **18**, 6076–6083.

34 P. M. Martins, P. Martins, V. Correia, J. G. Rocha and S. Lanceros-Mendez, Gd_2O_3:Eu nanoparticle-based poly (vinylidene fluoride) composites for indirect X-ray detection, *J. Electron. Mater.*, 2015, **44**, 129–135.

35 C. Hernandez, S. K. Gupta, J. P. Zuniga, J. Vidal, R. Galvan, H. Guzman, L. Chavez, K. Lozano and Y. Mao, High pressure responsive luminescence of flexible Eu^{3+} doped PVDF fibrous mats, *J. Mater. Sci. Technol.*, 2021, **66**, 103–111.

36 C. Liang, S. Zhang, L. Cheng, J. Xie, F. Zhai, Y. He, Y. Wang, Z. Chai and S. Wang, Thermoplastic membranes incorporating semiconductive metal-organic frameworks: an advance on flexible X–ray detectors, *Angew. Chem., Int. Ed.*, 2020, **59**, 11856–11860.

37 Y. Zhou, Q. Zhou, X. Niu, Z. Yan, T. Lin, J. Xiao and X. Han, Compositional engineering of doped zero-dimensional zinc halide blue emitters for efficient X-ray scintillation, *Inorg. Chem. Front.*, 2022, **9**, 2987–2996.

38 X. Ou, X. Qin, B. Huang, J. Zan, Q. Wu, Z. Hong, L. Xie, H. Bian, Z. Yi, X. Chen, Y. Wu, X. Song, J. Li, Q. Chen, H. Yang and X. Liu, High-resolution X-ray luminescence extension imaging, *Nature*, 2021, **590**, 410–415.

